Biosensors and Bioelectronics 141 (2019) 111443

Contents lists available at ScienceDirect

Biosensors and Bioelectronics

journal homepage: www.elsevier.com/locate/bios

Z-scheme I-BiOCl/CdS with abundant oxygen vacancies as highly effective cathodic material for photocathodic immunoassay

Hao Wang, Bihong Zhang, Jiajia Xi, Faqiong Zhao, Baizhao Zeng*

Key Laboratory of Analytical Chemistry for Biology and Medicine (Ministry of Education), College of Chemistry and Molecular Sciences, Wuhan University, Wuhan, 430072, PR China

ARTICLE INFO

Keywords:
Photocathodic immunosensor
Z-Scheme
Oxygen vacancies
Carcino embryonic antigen
Bismuth oxychloride
Cadmium sulfide

ABSTRACT

A novel label-free photocathodic immunosensor was constructed by introducing a direct Z-scheme I-BiOCl/CdS cathodic material as highly effective photocatalyst for the selective detection of carcino embryonic antigen (CEA). The Z-scheme photocatalyst could promote the separation of photogenerated carriers and showed a more negative conduction band potential. In addition, the I-BiOCl with abundant oxygen vacancies could activate electron acceptors (i.e. O_2 and H_2O_2) and made them reduce more completely, thus the sensitivity of the photocathodic immunosensor was significantly improved. Afterward, CEA antibody (Ab) was employed for the selective recognition of CEA target, which was covalently bonded to the substrate material. The formation of immune complexes hindered the diffusion of electron acceptors, thus the photocurrent decreased. Under the optimized conditions, the photocathodic immunosensor displayed abroad linear range (0.01–40.0 ng/mL) and a low detection limit (0.002 ng/mL) for CEA detection. Furthermore, acceptable reproducibility, excellent selectivity and high anti-interference ability were achieved. This work provides a new horizon for the design and development of Z-scheme cathodic materials as photoactive material for photocathodic biosensing.

1. Introduction

With the advantages of low cost, high sensitivity and rapid analysis, photoelectrochemical (PEC) bioanalysis platform has attracted much attention in enzymatic biosensors (Zhao et al., 2017), immunoassays (Zhao et al., 2018), aptamer sensors (Zhao et al., 2016) and DNA biosensors (Zhao et al., 2014). According to the electron transfer direction, PEC sensors can be classified into two types: anodic type and cathodic type (Li et al., 2018c). It is generally accepted that anodic PEC sensors suffer from poor anti-interference capability due to the strong oxidizing ability of photogenerated holes (Dai et al., 2017; Wang et al., 2015b; Zhang et al., 2018a). Unlike commonly used n-type semiconductors based photoanode, p-type semiconductor photocathodes preferentially react with the electron acceptors in the solution instead of the electron donors (Fan et al., 2018; Gong et al., 2016; Wang et al., 2014). On the other hand, the choice of suitable cathodic materials and design of the signal-amplified system will affect the sensitivity of cathodic PEC sensors (Gong et al., 2018; Tanne et al., 2011; Zhu et al., 2017). Generally, for cathodic PEC sensing, the more efficient reduction of electron acceptors, the larger cathodic photocurrent generated (Lv et al., 2017; Zhou et al., 2018). Therefore, in order to make the electron acceptors reduce more completely and rapidly, two important points should be considered: how to make the conduction band potential of cathodic materials decrease, and how to improve the activity of electron acceptors on the surface of cathodic materials. However, they have not been shed light on so far.

Photocatalysts with lower conduction band potentials can be obtained by creating a Z-scheme electron transfer process. In previous work, we synthesized direct Z-scheme cathodic materials BiOI-CdS (Wang et al., 2017a) and I-BiOCl/N-GQDs (Wang et al., 2018) (i.e., nitrogen doped graphene quantum dots) and constructed photocathodic sensors for the highly sensitive and specific detection of Cu^{2+} and chlorpyrifos, respectively. In the two systems, the resultant Z-scheme electron transfer process improved the separation of photogenerated carriers. By the way, a lower conduction band potential was achieved. Thus, the composites showed excellent PEC activity and large cathodic photocurrent signal. We notice that CdS is n-type semiconductor while I-BiOCl is p-type semiconductor, their matched energy levels are favorable for charge separation. More importantly, for CdS semiconductor electron is the majority carriers. The formation of Z-scheme electron transfer process benefits electron (on the conduction band of CdS) to transfer to the interface and to participate in the reduction reaction of electron acceptors.

Besides the effect of conduction band potential, the efficient

* Corresponding author.
E-mail address: bzzeng@whu.edu.cn (B. Zeng).

https://doi.org/10.1016/j.bios.2019.111443
Received 28 March 2019; Received in revised form 8 June 2019; Accepted 14 June 2019
Available online 19 June 2019
0956-5663/ © 2019 Elsevier B.V. All rights reserved.

reduction of electron acceptors is also closely related to their adsorption and activation on the cathodic materials. It is reported that abundant oxygen vacancies on the surface of photocatalysts can act as active sites (Li et al., 2018a; Zhang et al. 2018b, 2019). Especially, the oxygen vacancies are rich in localized electrons, which play a key role in the adsorption and activation of small molecules like H_2O, O_2, H_2O_2, N_2 and CO_2 (Aschauer et al., 2010; Bikondoa et al., 2006; Lee et al., 2011; Li et al., 2015; Li and Zhang, 2017). However, such an effect has seldomly been applied in photocathodic bioanalysis. It is worth mentioning that for a cathodic PEC sensor, O_2 and H_2O_2 usually act as electron acceptors (Gu et al., 2015; Shi et al., 2018; Wang et al., 2015a). Their activation by oxygen vacancies can greatly enhance the sensitivity of cathodic PEC sensors (Jiang et al., 2018; Li et al., 2017b; Zhang et al., 2018c). As far as we know, cathodic materials with abundant oxygen vacancies have not been reported for activating electron acceptors (i.e. O_2 and H_2O_2) and constructing photocathodic immunosensor.

In the present work, direct Z-scheme I-BiOCl/CdS composites were synthesized and used for constructing photocathodic immunoassay platforms. In this case, p-type semiconductor I-BiOCl with abundant oxygen vacancies acted as cathodic material, which was sensitized by n-type semiconductor CdS; O_2 and H_2O_2 acted as electron acceptors. The Z-scheme electron transfer process made the conduction band potential of cathodic material effectively decrease, while the abundant oxygen vacancies promoted the complete reduction of electron acceptors, thus amplified the detection signal. Upon the addition of CEA, immune complexes formed and the diffusion of electron acceptors was blocked, hence the cathodic photocurrent reduced.

2. Experimental section

2.1. Apparatus and reagents

The details of apparatus and reagents were shown in the supporting information.

2.2. Preparation of photocatalysts

I-BiOCl microspheres were synthesized according to previous work (Wang et al., 2018). I-BiOCl/CdS-*x* were prepared through one-pot precipitation method. Briefly, 700 mg I-BiOCl was added into 30 mL deionized water, after vigorous stirring for 0.5 h, equal volume of 0.10 M Na_2S aqueous solution and 0.10 M $CdCl_2$ solution were added. After another 0.5 h, the obtained product was washed for several times with deionized water and ethanol. Finally, the precipitate was dried at 60 °C overnight to obtain I-BiOCl/CdS-*x*. Different products were prepared by changing the dosage of CdS (*x*: the volume of $CdCl_2$ and Na_2S, x = 5, 10, 20, 30 mL). In addition, pristine CdS was synthesized under the same conditions but without I-BiOCl.

2.3. Fabrication of biosensor

The fabrication of photocathodic immunosensor is shown in Scheme 1. Firstly, 2 mg I-BiOCl/CdS-10 composite was dispersed in 1 mL 0.5% polyethyleneimine (PEI) solution to obtain a uniform suspension. The suspension (15 μL) was dropped onto a cleaned indium tin oxide (ITO) chip with a fixed area of 0.07 cm^2 and dried in an oven. Afterward, 5 μL 2.5% glutaraldehyde (GA) solution was dropped on it and the ITO chip was set aside for 1 h at room temperature. After rising with deionized water, 5 μL 10 μg/mL anti-CEA solution was coated on the modified layer and incubated for 12 h at 4 °C. After washing with Tris-HCl (pH 7.4) solution, 5 μL 1% bovine serum albumin (BSA, in 0.10 M pH 7.4 PBS) solution was added to block anti-CEA at 4 °C for 1 h, and then the modified ITO was thoroughly washed with Tris-HCl (pH 7.4) solution. Next, CEA solution with different concentrations was dropped onto the resulting electrode and incubated for 1 h at 37 °C, followed by rinsing and PEC measurement.

3. Results and discussion

3.1. Characterization of materials

The scanning electron microscope (SEM) images of the synthesized I-BiOCl, CdS and I-BiOCl/CdS-10 powders were shown in Fig. 1. The I-BiOCl microspheres were composed of lots of aligned nanoplates with thickness of several nanometers (Fig. 1A), while pure CdS nanoparticles extensively agglomerated (Fig. 1B). Fig. 1C revealed that CdS nanoparticles uniformly combined with I-BiOCl nanosheets. In order to obtain further information of the microstructure of I-BiOCl/CdS-10, high-resolution TEM (HRTEM) analysis was demonstrated (Fig. 1D and E). Lattice fringes with *d*-spacings of 0.336 and 0.84 nm could be ascribed to the (111) lattice plane of CdS and the (001) lattice plane of I-BiOCl, respectively (Jin et al., 2015; Wang et al., 2018). EDS mapping images were shown in Fig. 1F, indicating that the I-BiOCl/CdS-10 sample contained Bi, O, Cl, I, Cd and S elements. The introduction of CdS made the charge-transfer resistance (*R*ct) of the composite increase to some extent (Fig. S1). But the intimate contact between I-BiOCl and CdS was conducive to the electron transfer from I-BiOCl to CdS under photoexcitation. Hence, the separation efficiency of carriers was enhanced. In addition, in the X-ray photoelectron spectroscopy (XPS) survey spectrum of the I-BiOCl/CdS-10 sample, Bi, O, Cl, I, S and Cd signals were observed (Fig. 1G), which further confirmed the successful synthesis of I-BiOCl/CdS-10 composite.

3.2. Electrochemical and photoelectrochemical behaviors

Photocurrent of photoactive material is an effective parameter to measure the generation, separation and migration efficiency of photogenerated carriers (Huang et al., 2015). Herein, upon irradiation, the I-BiOCl/ITO electrode displayed a small cathodic photocurrent signal (Fig. 2A, curve a), CdS/ITO electrode represented a large anodic photocurrent, whereas the I-BiOCl/CdS-*x*/ITO electrode exhibited a larger cathodic photocurrent (Fig. 2A, curves b-e). When the dosage of CdS was low, the carrier generation was poor and the cathodic photocurrent signal was small. When it was high, the separation and migration of charges was suppressed, thus the cathodic photocurrent decreased. In this case, the I-BiOCl/CdS-10 displayed best photocatalytic performance.

The *I–V* characteristics of various photoelectrodes were tested from − 0.4 to + 0.1 V (vs Ag/AgCl) (Fig. 2B). It was observed that the cathodic photocurrent intensity of the I-BiOCl/CdS-10 was always higher than pure I-BiOCl within the tested potential range, owing to the effective spatial separation of electron-hole pairs. Electrochemical impedance spectroscopy (EIS) analysis was also performed to evaluate the PEC properties of photocatalysts (Fig. 2C). Clearly, the I-BiOCl/CdS-10 presented a much smaller semicircle diameter (equal to the electron-transfer resistance (Shang et al., 2019)) than pure I-BiOCl under irradiation, indicating the charge-transfer resistance lowered after introducing proper dosage of CdS. The higher photocurrent intensity and better conductivity were two important evidences to prove the enhanced PEC activity of I-BiOCl/CdS-10. This was related to the formation of Z-scheme electron transfer process, which could effectively suppress the recombination of the carriers (Wang et al., 2017a; Zeng et al., 2019).

To quantitatively measure the recombination behavior of photogenerated carriers, a normalized parameter *D* is introduced (Meng et al., 2013):

$$D = (I_t - I_{st})/(I_{in} - I_{st}) \quad (1)$$

where I_{in}, I_{st} and I_t are the initial, steady-state and time-dependent photocurrent, respectively. The transient time constant (τ) is defined as

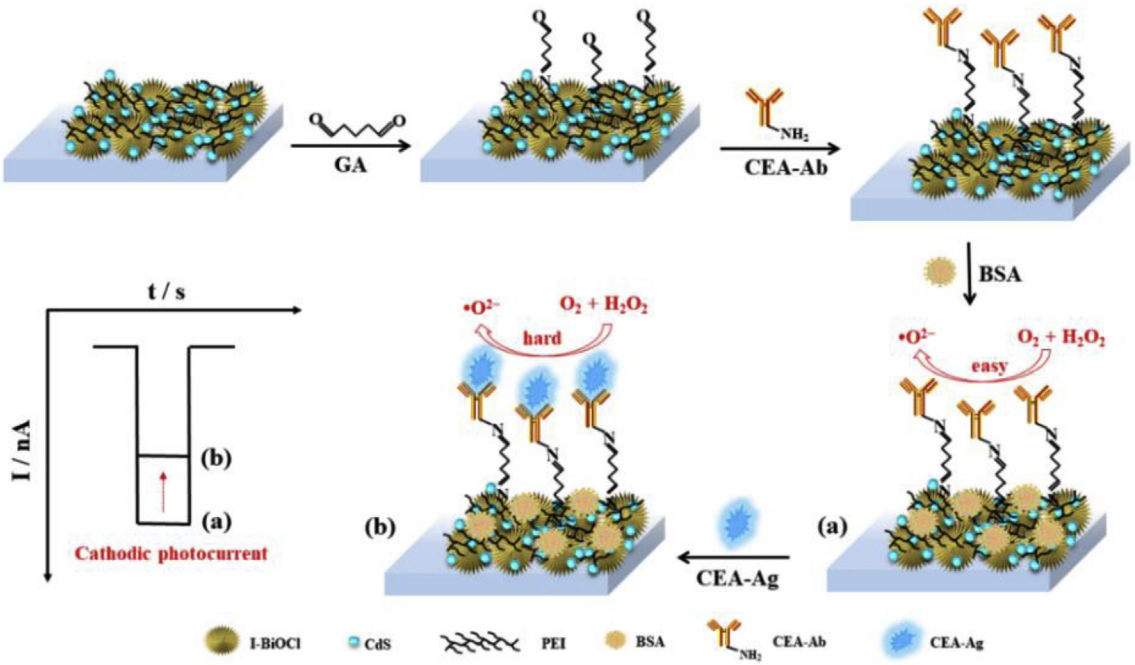

Scheme 1. Schematic illustration of photocathodic immunoassay of CEA based on direct Z-scheme I-BiOCl/CdS.

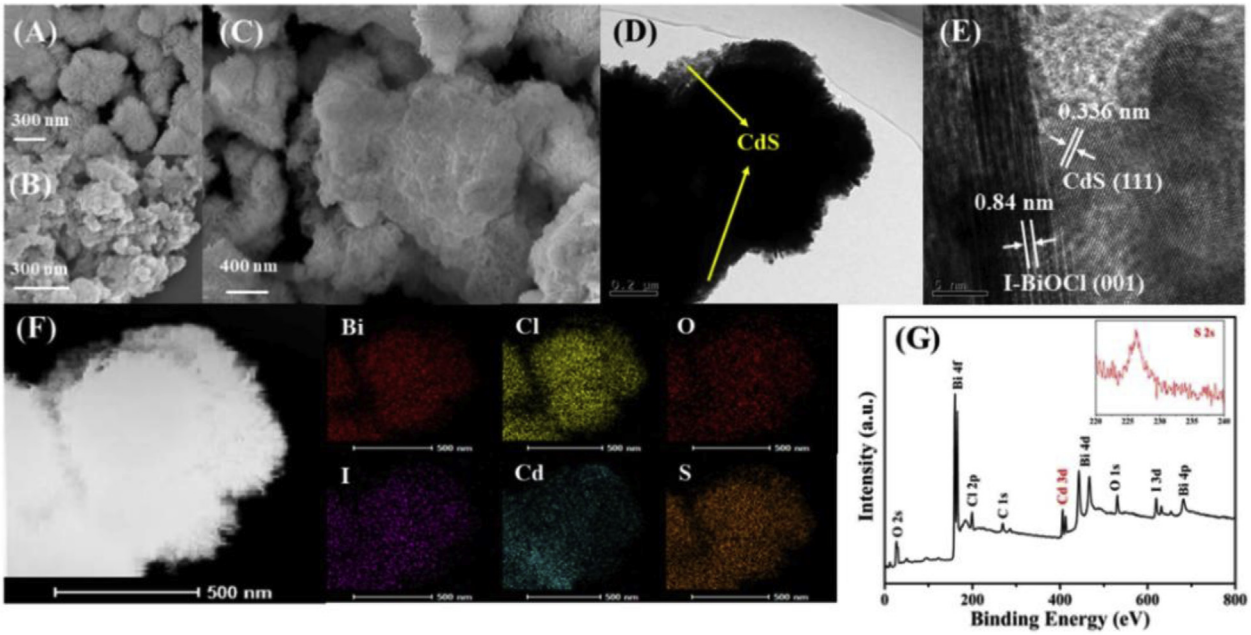

Fig. 1. SEM images of (A) I-BiOCl, (B) CdS, and (C) I-BiOCl/CdS-10. (D) TEM, (E) HRTEM, and (F) EDS mapping images of I-BiOCl/CdS-10. (G) XPS spectra of the I-BiOCl/CdS-10.

the time when ln D is equal to – 1, which reflects the general behavior of carrier recombination (Tayyebi et al., 2018). In Fig. 2D, the transient time constant is estimated to be 2.0 s for I-BiOCl and 3.7 s for I-BiOCl/CdS-10. The larger τ for the BiOCl/CdS-10 indicates that it has a lower charge recombination rate than pure I-BiOCl (Teng et al., 2016). In other words, more carriers can take part in the photocatalytic reaction. This is consistent with the previous *i-t* test result.

3.3. Optical characterization and mechanism of charge transfer

UV–vis diffuse reflectance spectrophotometry (DRS) is utilized to measure the light absorption characteristics and the band gap of I-BiOCl and CdS. As can be seen in Fig. 3A, the absorption edge of the samples shifts to longer wavelength monotonically and the absorption intensity increases as the CdS dosage increases, which indicates that the introduction of CdS can reduce the band gap and enhance the absorption of visible light. The band gap of samples can be calculated by the following formula (Zhang et al., 2014):

$$ahv = \mathrm{A}(hv - E_g)^{n/2} \quad (2)$$

where hv, E_g, A and α are light energy, band gap, constant value and absorption coefficient, respectively. The n values of I-BiOCl and CdS are 4 (direct transition) and 1 (indirect transition), respectively (Wang et al., 2017a; Wang et al., 2018). By extrapolating the straight portion

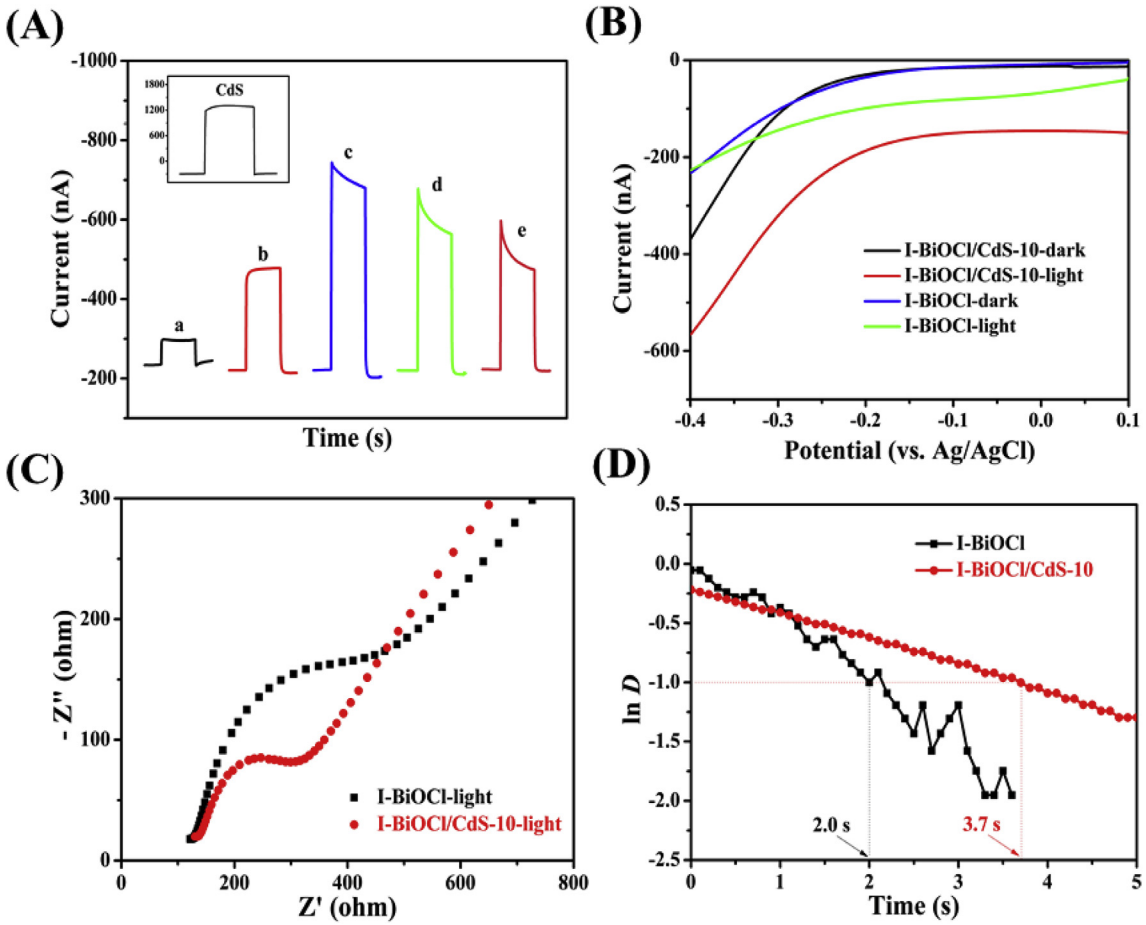

Fig. 2. (A) Photocurrent responses of I-BiOCl/ITO (a), I-BiOCl/CdS-*x*/ITO (*x* = 5, 10, 20, 30, from b to e) in 0.10 M Tris-HCl (pH 7.4) at the bias potential of – 0.1 V. Inset: the photocurrent response of CdS. (B) Linear sweep voltammograms of I-BiOCl/ITO and I-BiOCl/CdS-10/ITO under LED light (450 nm) illumination or not. (C) Nyquist plots of I-BiOCl/CdS-10/ITO and I-BiOCl/ITO with illumination. (D) Normalized plots of the *i-t* dependence for I-BiOCl/ITO and I-BiOCl/CdS-10/ITO.

of the $(ahv)^{1/2}$ or $(ahv)^2$ versus *hv* curves (Fig. 3B) to $\alpha = 0$, the band gaps of the I-BiOCl and CdS were obtained, and they were about 2.25 eV and 2.12 eV, respectively. The valence band (VB) edges of the I-BiOCl and CdS were characterized by XPS valence spectra, as illustrated in Fig. 3C. The positions of the valence band edges of I-BiOCl and CdS were determined to be 2.30 and 1.68 eV, respectively.

Based on the analysis of band energy levels and our previous research (Wang et al., 2017a; Wang et al., 2018), the possible charge transfer pathway between CdS and I-BiOCl is shown in Fig. 3D. Under irradiation, both I-BiOCl and CdS can be excited. The photogenerated electrons from the conduction band (CB) of I-BiOCl transfer to the valence band (VB) of CdS, then the adsorbed O_2 and H_2O_2 on the surface can accept electrons to produce $\bullet O_2^-$. The holes left on the VB of I-BiOCl are captured by the electrons of ITO electrode to generate cathodic photocurrent signal (Wang et al., 2018).

3.4. Mechanism discussion

Then, we conducted some experiments to verify the possible mechanism. To understand the role of O_2 and H_2O_2 in the system, the cathodic photocurrent responses of produced electrodes were recorded in Tris-HCl solution (pH 7.4) upon 450 nm illumination. As shown in Fig. 4A, when the solution was purged with highly pure nitrogen, the cathodic photocurrent response of I-BiOCl/CdS-10/ITO decreased significantly (curve a), demonstrating that the cathodic material I-BiOCl/CdS-10 was oxygen-sensitive and oxygen acted as electron acceptor (Shi et al., 2018; Yan et al., 2015). Upon the introduction of H_2O_2 (10.0 mM) in the deaerated solution, there was an obvious increase in photocurrent (curve c). These results showed that both O_2 and H_2O_2 acted as electron acceptors. Especially, when H_2O_2 was added into the air-saturated Tris-HCl (pH 7.4) buffer, as could be seen (curve d), a larger cathodic photocurrent occurred. Namely, H_2O_2 had greater impact on cathodic photocurrent than O_2. All these results clearly indicated that the fabricated photocathodes were O_2 and H_2O_2-sensitive, and O_2 and H_2O_2 acted as electron acceptors to promote separation of carriers, thus the cathodic photocurrent increased greatly (Dai et al., 2017; Tian et al., 2017).

As the main reduction product, $\bullet O_2^-$ radicals in the test system had been confirmed by electron spin resonance (ESR) measurement. As could be seen in Fig. 4B, the signal of $\bullet O_2^-$ radicals was enhanced after the addition of H_2O_2. Particularly, the peroxidase-like BiOX (X = Cl, Br, I) could catalyze the reducton of H_2O_2 to produce active radicals (Li et al., 2014; Ye et al., 2011; Zhang et al. 2018b, 2018c). Furthermore, the oxygen vacancies around the Bi^{3+} on the surface of I-BiOCl led to the formation of $Bi^{(+3-x)}$, which served as the active sites for the reduction of O_2 and H_2O_2 (Li et al., 2017a). ESR measurements provided auxiliary evidence for the existence of oxygen vacancies as an obvious ESR signal occurred at g = 2.003 (Jiao et al., 2017; Li et al., 2018b). Fig. 4C showed a strong characteristic ESR signal for the BiOI and BiOCl, revealing the existence of oxygen vacancies in these materials. Encouragingly, the I-BiOCl sample displayed slightly enhanced ESR signal, confirming that I-BiOCl possessed somewhat higher oxygen vacancies concentration compared with the pure BiOCl and BiOI samples. This phenomenon demonstrated that the doping of iodine ions in BiOCl was more conducive to the generation of oxygen vacancies.

Next, we studied the interaction between oxygen vacancies and

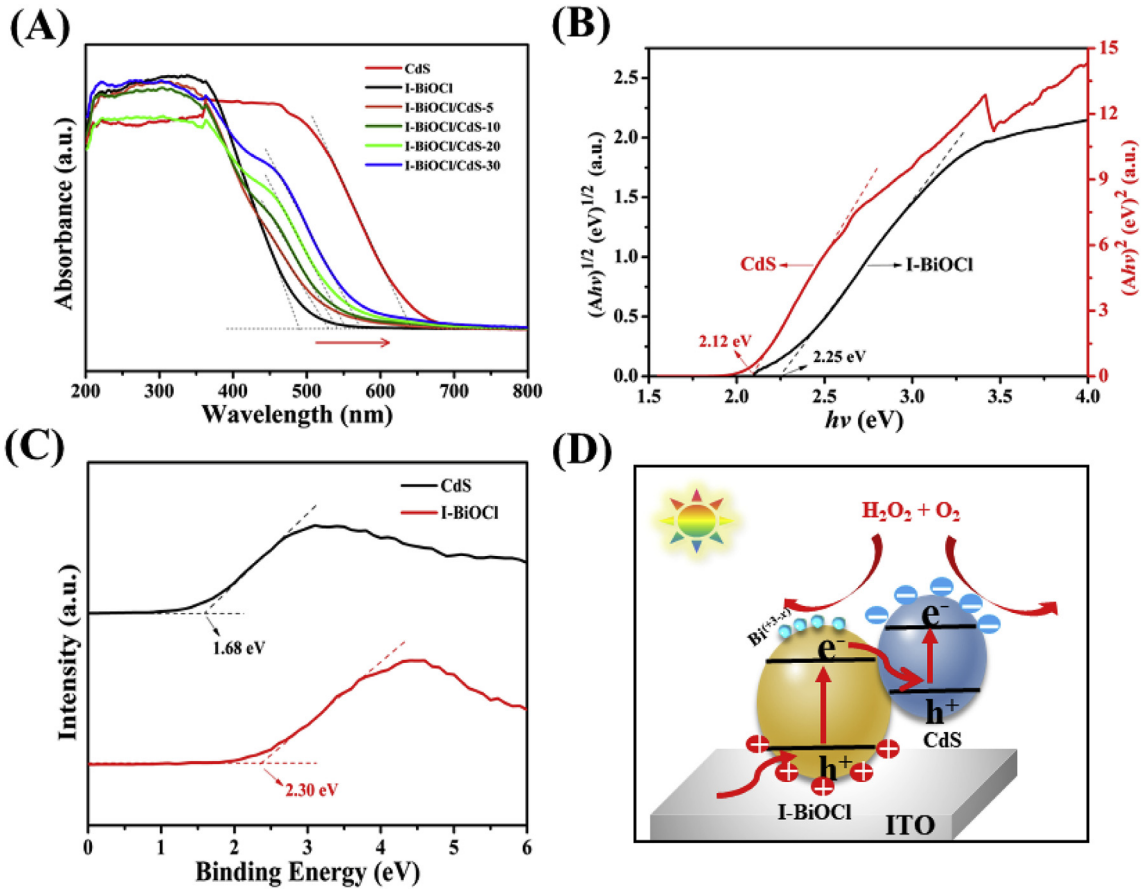

Fig. 3. (A) DRS of CdS, I-BiOCl and I-BiOCl/CdS-*x*. (B) Tauc plots and (C) valence band XPS spectra of CdS and I-BiOCl. (D) Schematic illustration of charge transfer pathway between CdS and I-BiOCl.

H_2O_2. Cyclic voltammetry (CV) was used to monitor the charge transfer at the interfacial region of photocatalysts/H_2O_2. Without H_2O_2, the electrodes exhibited small current signals (Fig. 4D). When H_2O_2 was present, the CV curve of I-BiOCl showed bigger reduction current (Fig. 4E). As I-BiOCl possessed more oxygen vacancies than BiOCl and BiOI, it could be deduced that oxygen vacancies served as active sites for the reduction of H_2O_2 (Wang et al., 2017b). In this case, the higher current intensity meant the higher capability of oxygen vacancies for the reduction of H_2O_2 (Li et al., 2017a; Zou et al., 2017). The EIS results further confirmed this point, as I-BiOCl showed a lowest charge-transfer resistance (Fig. 4F).

We also tested the amperometric *i–t* curves of H_2O_2 at – 0.1 V (vs Ag/AgCl) with or without irradiation. A bigger reduction current of H_2O_2 was acquired by PEC response (Fig. S2). This indicated H_2O_2 was mainly reduced by photocatalytic reaction rather than electrochemical reduction at – 0.1 V (vs Ag/AgCl).

3.5. Analytical performances

The influence of irradiation wavelength and the concentration of H_2O_2 was further studied. The result indicated the transient photocurrent of I-BiOCl/CdS-10/ITO under monochromatic light obviously decreased with increasing the wavelength and also matched well with its light absorption across the visible light region (Fig. S3). Considering the stability of photocurrent and the sensitivity of PEC sensor, 450 nm was chosen as the optimized irradiation wavelength. Moreover, the cathodic photocurrent intensity could be controlled by the concentration of H_2O_2. In Fig. S4, the cathodic photocurrent enhanced with the increase of H_2O_2 concentration. When the concentration exceeded 10.0 mM, the increase of photocurrent was not obvious. So, 10.0 mM was chosen as the optimized concentration.

In addition, we also examined the impact of applied potential, pH value and incubation time. As a result, the optimized applied potential was − 0.1 V, the optimized solution pH was 7.4 and the optimal incubation time was 60 min. The details were shown in supporting information (Fig. S5).

The fabrication of the photocathodic immunosensor was proved by recording the stepwise photocurrent responses (Fig. 5A), the cathodic photocurrent intensity significantly decreased after modifying GA (b), Ab (c), BSA (d) and CEA (e), because their steric hindrance affected the interfacial electron transfer. Under the optimized immunoassay conditions, the photocathodic immunosensor was used for the quantitative detection of CEA. As displayed in Fig. 5B, with increasing CEA concentration, the cathodic photocurrent of the electrode decreased. Furthermore, the cathodic photocurrent change ΔI ($\Delta I = I_{sample} - I_{blank}$) and the logarithmic value of CEA concentration showed a linear relationship in the range from 0.01 to 40.0 ng/mL, and the detection limit was 0.002 ng/mL. The linear regression equation was ΔI (nA) = 115.4 + 50.7 log C (ng/mL) (R^2 = 0.9950). Some recently reported methods for the detection of CEA were listed in Table S1 for comparison, and this photocathodic immunosensor displayed better analytical parameters.

For a photocathodic immunosensor, its stability is a key parameter. Fig. S6 exhibited the photocurrent responses of the photocathodic immunosensor with light switched on/off. Nearly no change in cathodic photocurrent was observed, which indicated the remarkable stability of the photocathodic immunosensor. Selectivity is also a very important criterion for a sensor. Here different kinds of interfering substances, such as dopamine, glucose, ascorbic acid, glutathione, lactate, uric acid, human epididymis protein (HE4), prostatic specific antigen (PSA) and

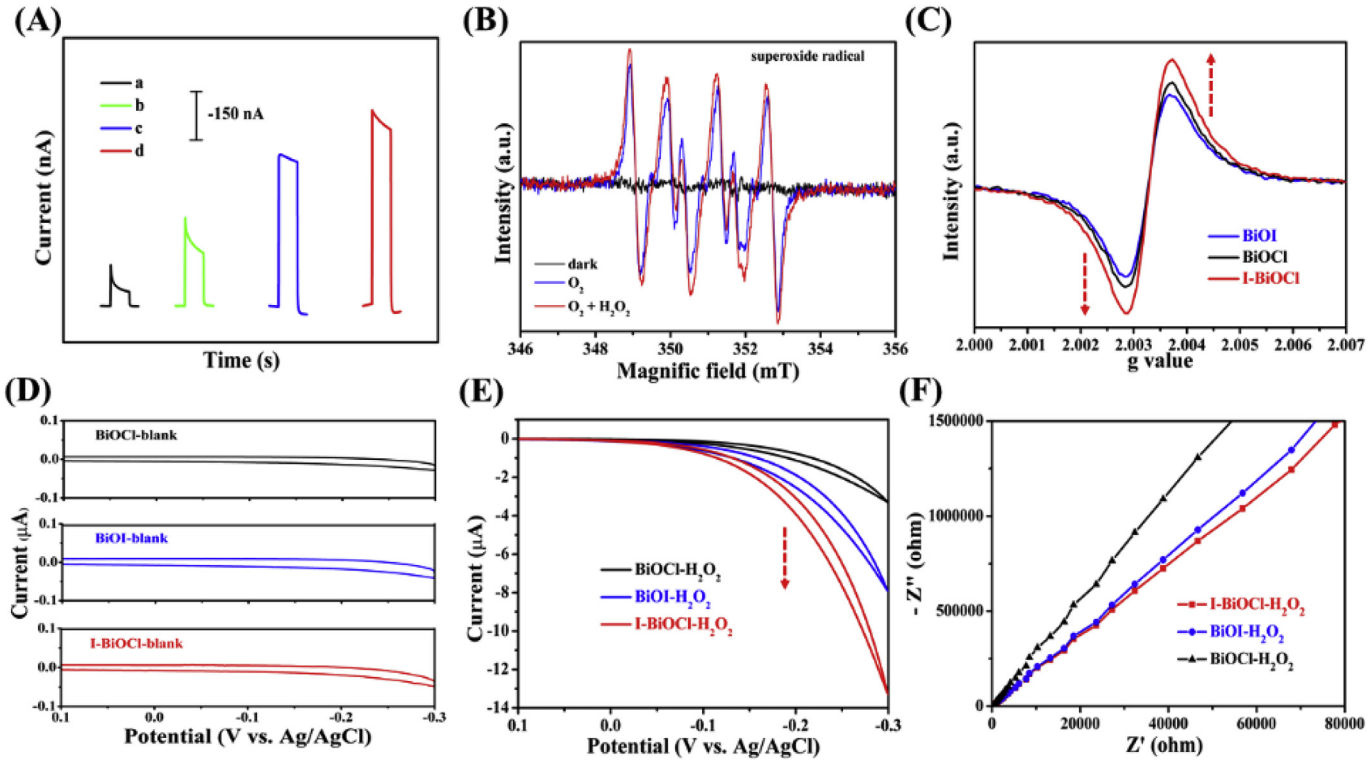

Fig. 4. (A) Photocurrent response of the I-BiOCl/CdS-10/ITO in (a) nitrogen-purged buffer, (b) air-saturated buffer, (c) (a) + H_2O_2, and (d) (b) + H_2O_2. (B) DMPO-$\cdot O_2^-$ trapping ESR spectra of I-BiOCl/CdS-10 (1 mg/mL) recorded in methanol and H_2O_2 (10.0 mM) solution. (C) ESR signals of oxygen vacancies. CV curves of BiOCl/ITO, BiOI/ITO and I-BiOCl/ITO in blank (D) and in nitrogen-purged buffer plus 10.0 mM H_2O_2 (E). (F) EIS of BiOCl/ITO, BiOI/ITO and I-BiOCl/ITO in Na_2SO_4 (0.10 M) electrolyte with H_2O_2 (10.0 mM).

alphafetoprotein (AFP) were chosen for the interference tests. As shown in Fig. 5C, no obvious cathodic photocurrent change appeared after mixing CEA with ten-fold of interfering substances or their mixture, indicating its better anti-interference capability. Besides, five electrodes were fabricated under the same conditions and used to test 0.05 ng/mL CEA (Fig. S7). As a result, a relative standard deviation (RSD) of 4.8% ($n = 5$) was obtained, indicating the PEC immunosensor had satisfactory reproducibility.

To evaluate its application feasibility, the photocathodic immunosensor was used for the detection of CEA in real sample. As shown in Fig. S8 and Table S2, the CEA concentration in serum sample was 1.20 ng/mL, and the recoveries were 94.0%–102.0%, indicating that the photocathodic immunosensor was promising for detecting CEA in serum sample. To confirm its accuracy, the measurement results were compared with the reference values obtained through a commercial CEA enzyme-linked immunosorbent assay (ELISA) kit (Table S3). As could be seen, they were in agreement with each other, the relative error was 5.5%. This indicated the developed method was quite reliable.

4. Conclusion

In this work, a simple photocathodic bioanalysis platform for the detection of CEA was designed and constructed, based on direct Z-scheme I-BiOCl/CdS cathodic material. The Z-scheme photocatalyst showed improved photogenerated-carriers separation and more

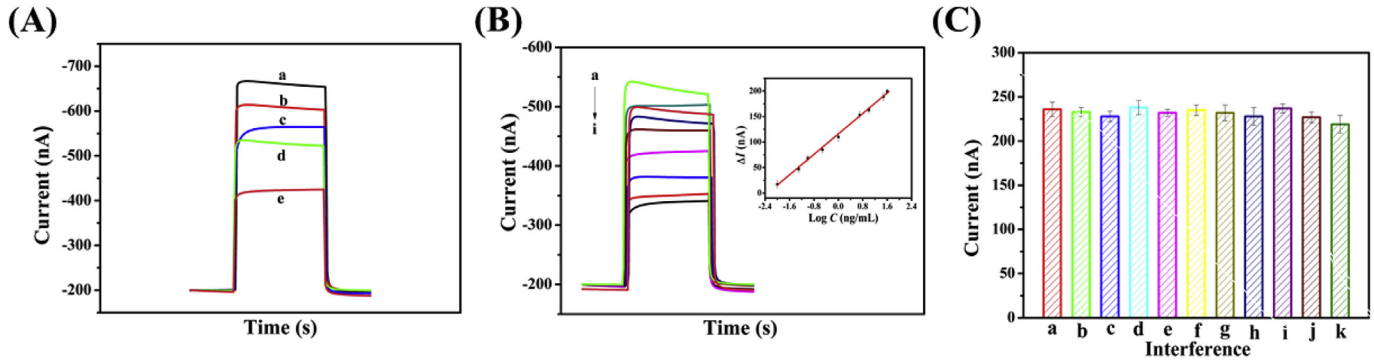

Fig. 5. (A) Photocurrent response curves corresponding to different fabrication steps: (a) I-BiOCl/CdS-10/PEI/ITO; (b) I-BiOCl/CdS-10/PEI/GA/ITO; (c) I-BiOCl/CdS. −10/PEI/GA/Ab/ITO; (d) I-BiOCl/CdS-10/PEI/GA/Ab/BSA/ITO; (e) I-BiOCl/CdS-10/PEI/GA/Ab/BSA/CEA/ITO. (B) Photocurrent responses of CEA. CEA concentrations (from a to i): 0.01, 0.05, 0.1, 0.3, 1.0, 5.0, 10.0, 30.0, 40.0 ng/mL; inset: the corresponding calibration curve of the photocathodic immunosensor. (C) Selectivity of the photocathodic immunosensor to CEA, (a) 1 ng/mL CEA; (b) (a) +10 fold dopamine; (c) (a) + 10 fold glucose; (d) (a) + 10 fold uric acid; (e) (a) + 10 fold ascorbic acid; (f) (a) + 10 fold glutathione; (g) (a) + 10 fold lactate; (h) (a) + 10 fold PSA; (i) (a) + 10 fold HE4; (j) (a) + 10 fold AFP; (k) (a) + mixture of the interfering substances.

negative conduction band potential; the I-BiOCl with abundant oxygen vacancies could activate electron acceptors (i.e. O_2 and H_2O_2) and made them reduce more completely. In addition, the anti-CEA had high recognition ability. Thus, the photocathodic immunosensor exhibited good analytical performance in terms of response time, selectivity, sensitivity and stability. The mechanism disclosed here highlighted the great potential of various cathodic materials as highly sensitive photoactive material in future photocathodic bioanalysis.

Declaration of interests

The authors declare that they have no known competing financial interests or personal relationships that could have appeared to influence the work reported in this paper.

CRediT authorship contribution statement

Hao Wang: Conceptualization, Methodology, Formal analysis, Investigation, Writing - original draft. **Bihong Zhang:** Formal analysis, Investigation, Writing - review & editing, Supervision. **Jiajia Xi:** Formal analysis, Investigation. **Faqiong Zhao:** Validation, Writing - review & editing, Supervision.

Acknowledgment

Financial support was from the National Natural Science Foundation of China (Grant No. 21675117).

Appendix A. Supplementary data

Supplementary data to this article can be found online at https://doi.org/10.1016/j.bios.2019.111443.

References

Aschauer, U., Chen, J., Selloni, A., 2010. Phys. Chem. Chem. Phys. 12, 12956–12960.
Bikondoa, O., Pang, C.L., Ithnin, R., Muryn, C.A., Onishi, H., Thornton, G., 2006. Nat. Mater. 5, 189–192.
Dai, W.X., Zhang, L., Zhao, W.W., Yu, X.D., Xu, J.J., Chen, H.Y., 2017. Anal. Chem. 89, 8070–8078.
Fan, G.C., Ma, L., Jayachandran, S., Li, Z., Luo, X., 2018. Chem. Commun. 54, 7062–7065.
Gong, L., Dai, H., Zhang, S., Lin, Y., 2016. Anal. Chem. 88, 5775–5782.
Gong, Y.T., Wu, X., Dong, Y., Liu, Q., Li, Z., Wang, G.L., 2018. Sens. Actuators, A B266, 408–415.
Gu, T.T., Wu, X.M., Dong, Y.M., Wang, G.L., 2015. J. Electroanal. Chem. 759, 27–31.
Huang, Y., Long, B., Li, H., Balogun, M.S., Rui, Z., Tong, Y., Ji, H., 2015. Adv. Mater. Interfaces 2, 1500249.
Jiang, X.Y., Zhang, L., Liu, Y.L., Yu, X.D., Liang, Y.Y., Qu, P., Zhao, W.W., Xu, J.J., Chen, H.Y., 2018. Biosens. Bioelectron. 107, 230–236.
Jiao, X., Chen, Z., Li, X., Sun, Y., Gao, S., Yan, W., Wang, C., Zhang, Q., Lin, Y., Luo, Y., Xie, Y., 2017. J. Am. Chem. Soc. 139, 7586–7594.
Jin, J., Yu, J., Guo, D., Cui, C., Ho, W., 2015. Small 11, 5262–5271.
Lee, J., Sorescu, D.C., Deng, X., 2011. J. Am. Chem. Soc. 133, 10066–10069.
Li, H., Li, J., Ai, Z., Jia, F., Zhang, L., 2018a. Angew. Chem. Int. Ed. 57, 122–138.
Li, H., Shang, J., Ai, Z., Zhang, L., 2015. J. Am. Chem. Soc. 137, 6393–6399.
Li, H., Shang, J., Yang, Z., Shen, W., Ai, Z., Zhang, L., 2017a. Environ. Sci. Technol. 51, 5685–5694.
Li, H., Zhang, L., 2017. Curr. Opin. Green Sustain. Chem. 6, 48–56.
Li, J., Wu, X., Pan, W., Zhang, G., Chen, H., 2018b. Angew. Chem. Int. Ed. 57, 491–495.
Li, L., Ai, L., Zhang, C., Jiang, J., 2014. Nanoscale 9, 4627–4634.
Li, R., Zhang, Y., Tu, W., Dai, Z., 2017b. ACS Appl. Mater. Interfaces 9, 22289–22297.
Li, Y., Chen, F., Luan, Z., Zhang, X., 2018c. Biosens. Bioelectron. 119, 63–69.
Lv, S., Zhang, K., Lin, Z., Tang, D., 2017. Biosens. Bioelectron. 96, 317–323.
Meng, F., Li, J., Cushing, S.K., Bright, J., Zhi, M., Rowley, J.D., Hong, Z., Manivannan, A., Bristow, A.D., Wu, N., 2013. ACS Catal. 3, 746–751.
Shang, H., Xu, H., Liu, Q., Du, Y., 2019. Sens. Actuators, B 289, 260–268.
Shi, X.M., Wang, C.D., Zhu, Y.C., Zhao, W.W., Yu, X.D., Xu, J.J., Chen, H.Y., 2018. Anal. Chem. 90, 9687–9690.
Tanne, J., Schafer, D., Khalid, W., Parak, W.J., Lisdat, F., 2011. Anal. Chem. 83, 7778–7785.
Tayyebi, A., Soltani, T., Hong, H., Lee, B.K., 2018. J. Colloid Interface Sci. 514, 565–575.
Teng, Q., Zhou, X., Jin, B., Luo, J., Xu, X., Guan, H., Wang, W., Yang, F., 2016. RSC Adv. 6, 36881–36887.
Tian, J., Zhu, H., Chen, J., Zheng, X., Duan, H., Pu, K., Chen, P., 2017. Small 13, 1700798.
Wang, G.L., Liu, K.L., Dong, Y.M., Wu, X.M., Li, Z.J., Zhang, C., 2014. Biosens. Bioelectron. 62, 66–72.
Wang, G.L., Liu, K.L., Shu, J.X., Gu, T.T., Wu, X.M., Dong, Y.M., Li, Z.J., 2015a. Biosens. Bioelectron. 69, 106–112.
Wang, G.L., Shu, J.X., Dong, Y.M., Wu, X.M., Zhao, W.W., Xu, J.J., Chen, H.Y., 2015b. Anal. Chem. 87, 2892–2900.
Wang, H., Ye, H., Zhang, B., Zhao, F., Zeng, B., 2017a. J. Mater. Chem. 5, 10599–10608.
Wang, H., Zhang, B., Zhao, F., Zeng, B., 2018. ACS Appl. Mater. Interfaces 10, 35281–35288.
Wang, J., Yang, B., Zhong, J., Yan, B., Zhang, K., Zhai, C., Shiraishi, Y., Du, Y., Yang, P., 2017b. J. Colloid Interface Sci. 497, 172–180.
Yan, K., Liu, Y., Yang, Y., Zhang, J., 2015. Anal. Chem. 87, 12215–12220.
Ye, L., Tian, L., Peng, T., Zan, L., 2011. J. Mater. Chem. 21, 12479–12484.
Zeng, R., Luo, Z., Su, L., Zhang, L., Tang, D., Niessner, R., Knopp, D., 2019. Anal. Chem. 91, 2447–2454.
Zhang, K., Lv, S., Lu, M., Tang, D., 2018a. Biosens. Bioelectron. 117, 590–596.
Zhang, L., Ruan, Y.F., Liang, Y.Y., Zhao, W.W., Yu, X.D., Xu, J.J., Chen, H.Y., 2018b. ACS Appl. Mater. Interfaces 10, 3372–3379.
Zhang, L., Zhu, Y.C., Liang, Y.Y., Zhao, W.W., Xu, J.J., Chen, H.Y., 2018c. Anal. Chem. 90, 5439–5444.
Zhang, L.J., Li, S., Liu, B.K., Wang, D.J., Xie, T.F., 2014. ACS Catal. 4, 3724–3729.
Zhang, N., Gao, C., Xiong, Y., 2019. J. Energy Chem. 37, 43–57.
Zhao, W.W., Xu, J.J., Chen, H.Y., 2016. TrAC Trends Anal. Chem. (Reference Ed.) 82, 307–315.
Zhao, W.W., Xu, J.J., Chen, H.Y., 2014. Chem. Rev. 114, 7421–7441.
Zhao, W.W., Xu, J.J., Chen, H.Y., 2017. Biosens. Bioelectron. 92, 294–304.
Zhao, W.W., Xu, J.J., Chen, H.Y., 2018. Anal. Chem. 90, 615–627.
Zhou, Q., Xue, H., Zhang, Y., Lv, Y., Li, H., Liu, S., Shen, Y., Zhang, Y., 2018. ACS Sens. 3, 1385–1391.
Zhu, Y., Xu, Z., Yan, K., Zhao, H., Zhang, J., 2017. ACS Appl. Mater. Interfaces 9, 40452–40460.
Zou, C., Yang, B., Bin, D., Wang, J., Li, S., Yang, P., Wang, C., Shiraishi, Y., Du, Y., 2017. J. Colloid Interface Sci. 488, 135–141.